Chemical Science

EDGE ARTICLE

View Article Online
View Journal

Check for updates

Cite this: DOI: 10.1039/d6sc00648e

All publication charges for this article have been paid for by the Royal Society of Chemistry

Band-bending engineering in Cu_2ZnSnS_4 photocathodes using a composite (Zn,Ti)O electron transport layer for solar water splitting

Siyuan Ren, Muhammad Abbas,* Zhibin Xie, Zilin Lu, Jasim Yousaf, Muhammad Ishaq, Zhuanghao Zheng, Jun Zhao, Shuo Chen* and Guangxing Liang*

Received 23rd January 2026
Accepted 21st April 2026

DOI: 10.1039/d6sc00648e

rsc.li/chemical-science

The development of efficient and stable photocathodes from earth-abundant materials is a critical challenge for photoelectrochemical (PEC) hydrogen production. While Cu_2ZnSnS_4 (CZTS) is a promising absorber due to its ideal bandgap and non-toxic constituents, its performance is plagued by severe interfacial recombination. This work addresses this limitation through the precise engineering of a zinc-titanium oxide (Zn,Ti)O electron transport layer (ETL) in Mo/CZTS/CdS/(Zn,Ti)O/Pt photocathodes. We systematically investigate the influence of atomic-layer-deposited (Zn,Ti)O on the heterojunction's microstructure, band alignment, and charge transfer kinetics. A suite of characterization studies reveals that a suitable ETL thickness forms a dense, conformal coating and establishes an optimal spike-like conduction band offset at the CdS/(Zn,Ti)O interface, which minimizes bulk and interfacial charge-transfer resistance. Consequently, the optimized photocathode achieves a remarkable photocurrent density of 29.2 mA cm^{-2} at 0 V_{RHE} and a high half-cell solar-to-hydrogen efficiency (HC-STH) of 7.02%. This study demonstrates that fine control of composite ETLs is a powerful strategy to unlock the potential of CZTS and related earth-abundant absorbers for scalable solar fuel production.

1. Introduction

Nowadays, the growing demand for fossil fuels is accelerating their depletion, while greenhouse gas emissions are constantly increasing.[1,2] This situation has made the world more eager to find clean and sustainable energy sources. Molecular hydrogen, due to its high weight energy density and compatibility with various conversion technologies, is widely regarded as a promising carbon-free fuel. Yet, industrial hydrogen production still relies predominantly on fossil-fuel-based processes such as steam methane reforming, which are energy intensive and emit large quantities of CO_2. To fully realize the environmental benefits of a "hydrogen economy", it is essential to develop technologies that can generate hydrogen directly from renewable primary energy sources, particularly solar energy.[3] Photoelectrochemical (PEC) water splitting,[4,5] first demonstrated on a TiO_2 photoelectrode in 1972,[6] offers an elegant approach to solar hydrogen production by integrating light harvesting, charge separation, and interfacial redox reactions within a single device.[7] Compared with photovoltaic electrolysis or granular photocatalysts,[8] integrated PEC cells can reduce the complexity of the system, decrease resistance losses, and potentially achieve a compact modular architecture. In PEC devices, the photocathode is generally composed of a p-type semiconductor absorption layer and an n-type electron transport layer, which play a core role in driving the hydrogen evolution reaction.[9] The light absorption properties of the photocathode, the position of the band edge, the nature of carrier transport and the condition of interface defects, these factors together determine the achievable photocurrent density, initial potential and the efficiency of solar hydrogen production. However, the development of photoelectrode materials that simultaneously possess high efficiency, high current density, and simple preparation methods is a central challenge for their practical, commercial-scale application.[10]

Among the various photocathode materials explored, Cu-based chalcogenides have attracted particular interest due to their suitable bandgaps, strong visible-light absorption coefficients, and compositional flexibility. $Cu(In,Ga)Se_2$ (CIGS), for example, has reached a half-cell STH efficiency of 9.3%.[11] However, the scarcity and high cost of indium and gallium fundamentally limit the scalability of CIGS-based PEC systems. Similarly, antimony selenide (Sb_2Se_3) exhibits advantages in low toxicity and cost-effectiveness but suffers from performance

---

Institute of Thin Film Physics and Applications, Shenzhen Key Laboratory of Advanced Thin Films and Applications, Key Laboratory of Optoelectronic Devices and Systems of Ministry of Education and Guangdong Province, State Key Laboratory of Intelligent Construction and Healthy Operation and Maintenance of Deep Underground Engineering, College of Physics and Optoelectronic Engineering, Shenzhen University, Shenzhen, 518060, China. E-mail: abbas.cssp@hotmail.com; chensh@szu.edu.cn; lgx@szu.edu.cn

limitations due to band misalignment with its ETL.[12,13] In contrast, the kesterite compound Cu_2ZnSnS_4 (CZTS) is composed exclusively of earth-abundant and non-toxic elements, while retaining many of the desirable optoelectronic attributes of CIGS. CZTS exhibits a direct bandgap of ~1.5 eV, a conduction band minimum close to the H^+/H_2 redox potential, and an absorption coefficient exceeding $>10^4$ cm^{-1},[14,15] supporting a theoretical photocurrent density above 30 mA cm^{-2} under AM 1.5G illumination. These features render CZTS an appealing platform for cost-effective, environmentally benign PEC photocathodes. Despite this promise, state-of-the-art CZTS photocathodes still operate far below their theoretical limits. Two bottlenecks are particularly critical. First, the CZTS absorber inherently suffers from deep-level recombination centers, including Cu_{Zn} antisite defects and Cu vacancies, which introduce mid-gap states and drastically shorten carrier lifetimes.[16] Second, the heterojunction formed between CZTS and the ETL often exhibits suboptimal band alignment and high densities of interfacial defects, leading to severe electron–hole recombination at or near the junction. These loss mechanisms manifest macroscopically as reduced photovoltage, incomplete charge collection, and poor fill factor in PEC J–V characteristics. Consequently, the rational design of ETLs that can simultaneously tailor band alignment, extract electrons efficiently, and passivate interfacial defects is essential for unleashing the full potential of CZTS.

Conventional ETL materials present inherent trade-offs when integrated with CZTS/buffer. Titanium dioxide (TiO_2), while chemically robust and non-toxic, possesses a wide bandgap (~3.2 eV) and relatively high resistivity,[17] leading to poor electrical coupling with CZTS and sub-optimal electron extraction.[18] Transparent conductive oxides such as indium tin oxide (ITO) offer high conductivity but rely on scarce indium and do not adequately address interfacial recombination at the chalcogenide surface.[19] To overcome these limitations, composite oxide ETLs that combine the advantages of multiple constituents have emerged as a promising alternative.[20] In this context, zinc-titanium oxide ((Zn,Ti)O) is particularly attractive. First, the ZnO component features high electron mobility,[21] the Ti^{4+} ions substituted for Zn^{2+} sites acts as a donor, providing two free electrons per dopant and increasing the carrier concentration. This results in a film conductivity substantially higher than that of intrinsic ZnO,[22,23] enabling rapid lateral and vertical transport of photogenerated electrons away from the CZTS/(Zn,Ti)O interface, which helps to mitigate bulk and interfacial recombination.[24] Second, the high electron extraction capability of (Zn,Ti)O facilitates the swift removal of photogenerated electrons from the CdS layer, reducing hole accumulation. This kinetically suppresses photocorrosion and enhances the device performance. Additionally, the (Zn,Ti)O interface effectively passivates defect states, reducing trap-assisted recombination.[25] By appropriately tuning the thickness of (Zn,Ti)O, it is possible to achieve electrical conductivities several orders of magnitude higher than pure TiO_2, maintain high visible-light transparency,[26,27] and exhibit a bandgap and electron affinity compatible with the formation of a desirable spike-type conduction band offset at the CZTS/CdS/(Zn,Ti)O interfaces. Although these advantages are conceptually clear, the PEC performance of CZTS/CdS/(Zn,Ti)O photocathodes is extremely sensitive to the thickness and microstructure of the ETL. In addition, the composition, defect state and the position of the band edge will have some subtle changes with the thickness. Therefore, systematically designing the thickness and deeply studying the mechanism involved are very crucial for determining the optimal (Zn,Ti)O configuration. Such a configuration can strike a balance in terms of coverage, electrical conductivity, optical transparency and band alignment.

In this work, we constructed a Mo/CZTS/CdS/(Zn,Ti)O/Pt photocathode architecture in which the thickness of the novel (Zn,Ti)O ETL is precisely controlled at 10, 20 and 30 nm *via* atomic layer deposition. By correlating PEC performance with ETL thickness and combining comprehensive structural, spectroscopic, electrical, and interfacial analyses, we systematically elucidate the role of ETL thickness in governing band alignment, interfacial energetics, and charge-carrier transport within the photocathode. The results show that a 20 nm (Zn,Ti)O layer yields dense, pinhole-free coverage, an optimized surface potential distribution at CZTS/CdS grain boundaries, significantly reduced bulk and interfacial charge-transfer resistances, and a favorable spike-like conduction band offset (+0.10 eV) at the CdS/(Zn,Ti)O interface. These synergistic effects result in a champion photocurrent density of 29.2 mA cm^{-2} at 0 V_{RHE} and an HC-STH efficiency of 7.02%.

2. Experimental section

2.1. Preparation of materials

All reagents were used as received without further purification. Cuprous chloride (CuCl, ≥99.95%), zinc acetate dihydrate ($C_4H_6O_4Zn\cdot 2H_2O$, 99.99%), stannic chloride pentahydrate ($SnCl_4\cdot 5H_2O$, 99.99%) and 2-methoxyethanol ($C_3H_8O_2$, ≥99.7%) were purchased from Aladdin. Tin(II) sulfide (SnS, 99%), sublimed sulfur (S, 99.95%), aqueous ammonia (NH_3), cadmium sulfate ($CdSO_4$, 99%), thiourea (CH_4N_2S, ≥99%) and titanium(IV) chloride ($TiCl_4$, ≥99%) were obtained from Sigma-Aldrich. Deionized water was used in all aqueous processes.

2.2. Synthesis of the CZTS absorber layer

CZTS thin films were fabricated *via* a solution-processed spin-coating method. A metal-thiourea precursor solution was prepared by dissolving CuCl, zinc acetate dihydrate, $SnCl_4\cdot 5H_2O$, and thiourea in 2-methoxyethanol under vigorous stirring until a clear yellow solution was obtained. Additional 2-methoxyethanol was then introduced, and the mixture was filtered to remove any precipitates. The resulting precursor solution was spin-coated onto thoroughly cleaned molybdenum-coated soda-lime glass substrates at 4000 rpm for 30 s per cycle. After each deposition, the films were annealed on a hot plate in air at 290 °C for 150 s. The as-deposited precursor films were subsequently sulfurized in a tube furnace. Multiple CZTS coated substrates were loaded into a sealed graphite box together with sublimed sulfur and SnS powders, serving as the sulfur and tin sources, respectively. The graphite box was placed at the center of a quartz tube and heated in a two-step profile: first to 80 °C at a ramp rate of 4 °C s^{-1}, followed by heating to 620 °C at 5 °C s^{-1}. The temperature was held at 620 °C for 20 min, after which the furnace was switched off to allow natural cooling to room temperature. Following this process, polycrystalline CZTS absorber layers were obtained.

2.3. Fabrication of CZTS/CdS/(Zn,Ti)O/Pt photocathodes

After formation of the CZTS absorber, a CdS buffer layer was deposited by chemical bath deposition (CBD). In a glass beaker, deionized water, NH_3 solution, thiourea and $CdSO_4$ were mixed in sequence under constant stirring. SLG/Mo/CZTS substrates were immersed vertically in the bath, which was then heated to 80 °C and kept for 8.5 min. The samples were collected, rinsed thoroughly with deionized water and dried in an oven, yielding SLG/Mo/CZTS/CdS stacks. Electron transport layers of (Zn,Ti)O were subsequently deposited onto the CZTS/CdS films by atomic layer deposition (ALD). Diethyl zinc (DEZ), $TiCl_4$ and deionized water served as precursors for Zn, Ti and (Zn,Ti)O, respectively. The DEZ and H_2O reservoirs were maintained at room temperature, whereas the $TiCl_4$ container, precursor delivery lines and reaction chamber were held at 65, 100 and 190 °C, respectively. One ALD cycle consisted of a DEZ (or $TiCl_4$) pulse, an H_2O pulse and N_2 purging after each precursor exposure. The cycle sequence was repeated until the desired (Zn,Ti)O thicknesses were obtained; the resulting films with nominal thicknesses of 10, 20 and 30 nm are referred to as PC-1, PC-2 and PC-3, respectively. Additionally, 12 independent photocathode devices were fabricated for each of PC-1, PC-2 and PC-3 for subsequent statistical performance characterization. Ti incorporation into the ZnO matrix was controlled by periodically introducing $TiCl_4/H_2O$ sub-cycles during the ALD process. Finally, a thin Pt co-catalyst layer was sputtered onto the ETL surface using a 108 Auto Sputter Coater operated at 20 mA DC for 50 s. The resulting photocathode architecture can thus be denoted as SLG/Mo/CZTS/CdS/(Zn,Ti)O/Pt. Silver paste was applied to the back of the already exposed Mo, which was done to form a reliable ohmic contact for the subsequent photoelectrochemical measurement.

2.4. Photoelectrochemical measurements

The PEC performance of the devices was evaluated on a CHI 660E electrochemical workstation using the traditional three-electrode configuration. Here, SLG/Mo/CZTS/CdS/(Zn,Ti)O/Pt was used as the working electrode, a Pt rod was used as the counter electrode, and an Ag/AgCl electrode was used as the reference electrode. All tests were carried out in 0.5 M H_2SO_4 aqueous electrolyte (pH $\approx$ 1). A 150 W xenon lamp equipped with an AM 1.5G filter was used as the illumination source and calibrated to 100 mW cm^{-2} using a certified Si reference cell. Linear sweep voltammetry (*J*–*V* curves) was performed at a scan rate of 20 mV s^{-1} under chopped or continuous illumination as specified. The PEIS test was carried out under simulated sunlight over the frequency range 10–10^4 Hz. ZView software was used to carry out the analysis and fitting of impedance spectra. Capacitive voltage measurements were conducted at a frequency of 1000 Hz to extract the flat band potential and estimate the majority carrier density of the CZTS absorber.

2.5. Structural and electronic characterization studies

The crystal structure and phase purity of the CZTS-based films were characterized by X-ray diffraction (XRD, Rigaku Ultima-IV) using Cu Kα radiation. Surface and cross-sectional morphologies were examined using field-emission scanning electron microscopy (FE-SEM, Zeiss SUPRA 55). Local surface potentials and contact potential differences were mapped *via* Kelvin probe force microscopy (KPFM, Bruker Dimension ICON). Optical properties, including reflectance and transmission, were measured with a Shimadzu UV-3600 spectrophotometer to determine the band gap. Furthermore, the electronic structure was probed by ultraviolet photoelectron spectroscopy (UPS, PHI 5000 VersaProbe) employing a He I (21.2 eV) source to determine the work function and valence band maximum position. Together, these techniques provide a comprehensive view of the structural, morphological, optical, and electronic properties essential for understanding the PEC performance of the fabricated heterostructures.

3. Results and discussion

To understand the influence of ETL thickness on the photoelectrochemical performance of CZTS photocathodes, Mo/CZTS/CdS/(Zn,Ti)O/Pt architectures were fabricated with (Zn,Ti)O thicknesses of 10, 20 and 30 nm, and these photocathodes were named PC-1, PC-2 and PC-3, respectively. A standard three electrode system was used to test the as prepared photocathodes under AM 1.5G simulated sunlight intensity (100 mW cm^{-2}) illumination in 0.5 M H_2SO_4 (electrolyte) as depicted in the schematic in Fig. 1a. Fig. 1b shows the current density–voltage (*J*–*V*) curves of all devices under dark conditions and continuous simulated sunlight illumination. The results indicate that the PC-2 device with a 20 nm-thick (Zn,Ti)O layer exhibits a photocurrent density of 29.20 mA cm^{-2} at 0 V, which is significantly higher than that of PC-1 (16.15 mA cm^{-2}) and PC-3 (23.74 mA cm^{-2}). Meanwhile, the chopped-light *J*–*V* measurement results (Fig. 1c) further demonstrate that the PC-2 device presents the highest and most stable photocurrent response. Furthermore, the dark current measured for the PC-1 and PC-2 samples was negligible, approaching zero, which confirms the absence of significant parasitic electrochemical reactions during testing.

In contrast, the slightly higher dark current observed for PC-3 may be attributed to minor parasitic reactions. Fig. 1d intuitively shows the vigorous evolution of hydrogen bubbles on the photocathode surface, which visually confirms the practical PEC activity of the devices. All potentials measured against the Ag/AgCl reference electrode were converted to the reversible hydrogen electrode (RHE) scale *via* the Nernst equation. These values were then used to calculate the HC-STH efficiency:[28]

$$\text{HC-STH}\ (\%) = J_{\text{ph}} \times (V_{\text{RHE}} - V_{\text{H}^+/\text{H}_2})/P_{\text{sun}} \times 100\% \quad (1)$$

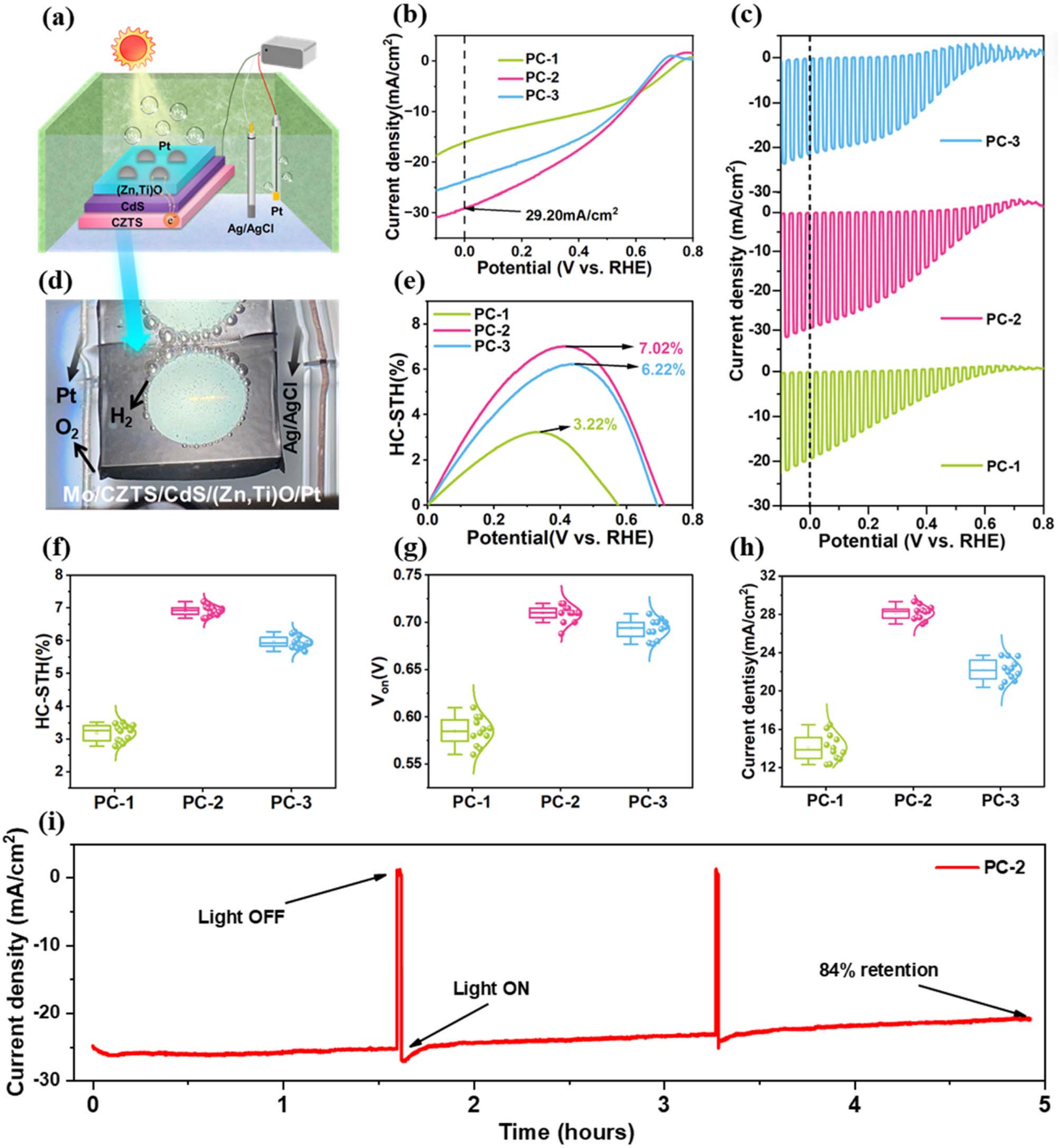

Fig. 1 PEC performance of CZTS-based photocathodes. (a) Schematic diagram of the three-electrode PEC measurement configuration. (b) *J*–*V* curves of Mo/CZTS/CdS/(Zn,Ti)O/Pt photocathodes with (Zn,Ti)O thicknesses of 10, 20, and 30 nm under continuous light illumination. (c) Chopped *J*–*V* curves of the same photocathodes under chopped AM 1.5G simulated sunlight. (d) Photograph of hydrogen bubbles generated on the photocathode surface in the electrolyte. (e) Calculated HC-STH conversion efficiencies. Statistical distributions of (f) HC-STH efficiencies, (g) onset potentials, and (h) photocurrent densities of the devices (12 independent devices per batch). (i) Stability test of the PC-2 photocathode under AM 1.5G illumination, 0 V *vs.* RHE, and 0.5 M H_2SO_4 (pH 1) electrolyte conditions.

$$V_{\mathrm{RHE}} = V_{\mathrm{Ag/AgCl}} + 0.059 \times \mathrm{pH} \tag{2}$$

where $V_{\mathrm{H^+/H_2}}$ is the reduction potential for hydrogen (0 V_{RHE}), V_{RHE} is the potential relative to the RHE, and P_{sun} is the intensity of simulated sunlight (100 mW cm^{-2}). The as calculated HC-STH efficiencies for the PC-1, PC-2 and PC-3 devices are shown in Fig. 1e. The PC-2 device reached the maximum value of 7.02% at 0.42 V_{RHE} which is significantly higher than comparative PC-1 (3.22%) and PC-3 (6.22%) devices. In parallel, a statistical comparison of the PEC performance of the devices

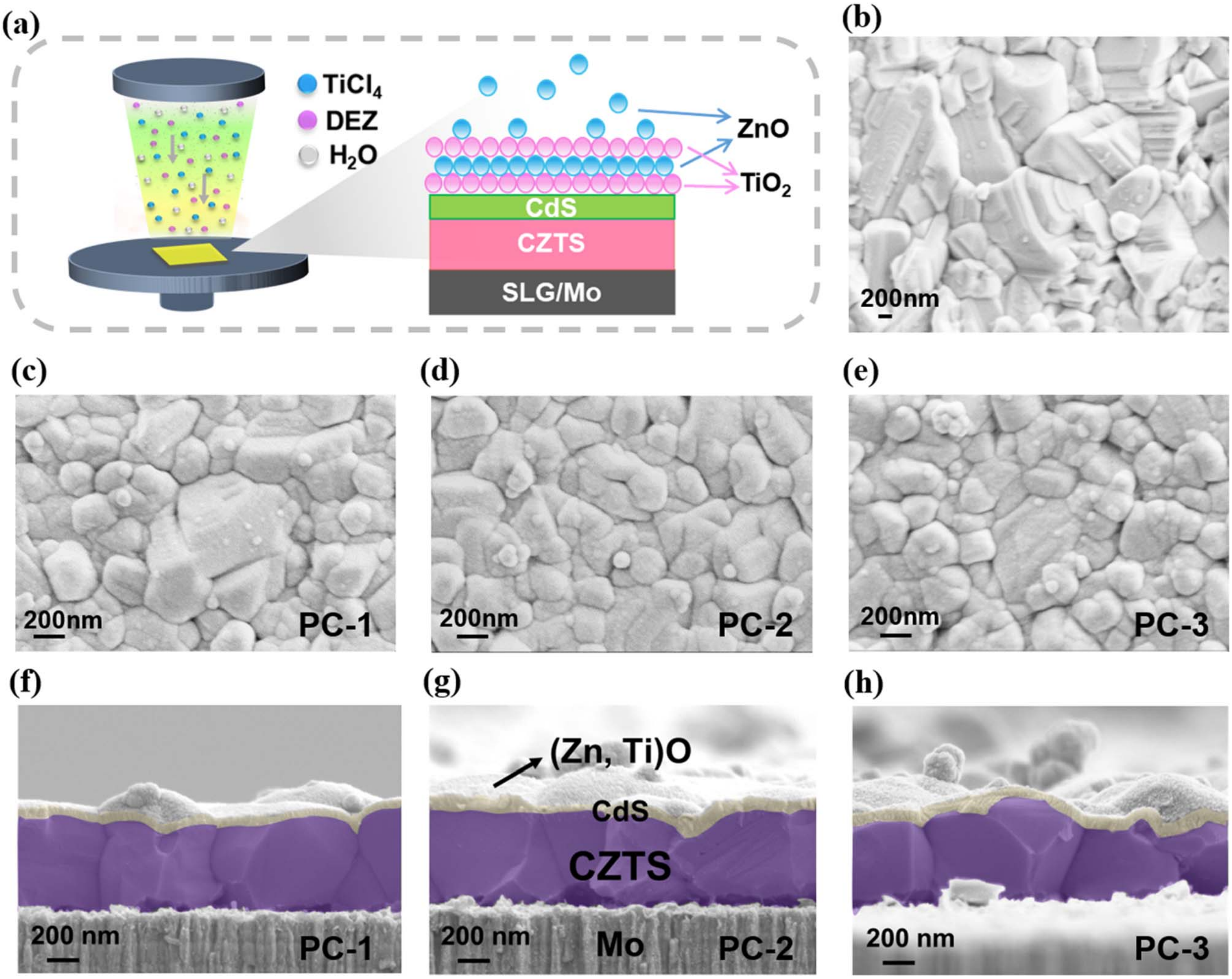

Fig. 2 Microstructural analyses. (a) Atomic layer deposition (ALD) process for ETL preparation. (b) Plan-view SEM image of the CZTS absorber thin film. (c–e) Surface SEM images of CZTS/CdS/(Zn,Ti)O photocathodes with (Zn,Ti)O thicknesses of 10, 20, and 30 nm, respectively. (f–h) Cross-sectional SEM images of the corresponding CZTS/CdS/(Zn,Ti)O stacks.

(Fig. 1f–h) shows that the PC-2 device consistently delivers the highest stable HC-STH efficiency (Fig. 1f), the most favorable onset potential V_{on} (Fig. 1g), and the highest photocurrent density (Fig. 1h), with narrow distributions, indicating good reproducibility. This analysis reveals the excellent reproducibility and performance of our champion PC-2 device (Fig. 1f–h). Gas chromatography (GC) was used to measure the evolution of H_2 and O_2 *in situ*, thus evaluating the photon utilization capability and faradaic efficiency (FE) of the champion PC-2 photocathode (Fig. S1). The PC-2 photocathode achieves continuous H_2 and O_2 evolution at rates of 2.50 μmol min^{-1} and 1.75 μmol min^{-1}, respectively. A high faradaic efficiency of 85.2% for H_2 evolution is obtained, indicative of negligible parasitic side reactions or competing redox processes on the photocathode surface. After 1 h of continuous irradiation, the PC-2 photocathode generates a cumulative amount of approximately 128 μmol of H_2 and 63 μmol of O_2, further confirming the efficient photon utilization for photoelectrochemical solar water splitting. In addition to developing a highly efficient photocathode, evaluating its long-term PEC operational stability is crucial for practical solar water splitting applications. Fig. 1i presents the stability of the champion PC-2 photocathode measured at 0 V_{RHE} for ≈5 hours under continuous AM 1.5G light irradiation in 0.5 M H_2SO_4 electrolyte (pH 1). The champion PC-2 photocathode exhibits remarkable long-term stability, retaining approximately ≈84% of its initial J_{ph} after the ≈5 hours of operation.

The schematic in Fig. 2a illustrates the atomic layer deposition (ALD) process used to deposit (Zn,Ti)O onto the CZTS/CdS absorber. To comprehensively verify the crystalline phases of all key components and the elemental composition of the (Zn,Ti)O ETL, XRD and energy-dispersive X-ray spectroscopy (EDS) characterization studies were performed. The XRD pattern (Fig. S2a) exhibits distinct diffraction peaks corresponding to chalcopyrite CZTS, hexagonal CdS, and amorphous (Zn,Ti)O, with no impurity phases detected, confirming the structural integrity and phase purity of the CZTS/CdS/(Zn,Ti)O heterostructure. Furthermore, XPS characterization of the

(Zn,Ti)O ETL is reported in our previous work,[25] with the same ALD deposition process adopted in this study, confirming the chemical states of Zn and Ti. The EDS results in Fig. S3 further authenticate the elemental composition (Zn, Ti, and O) of the (Zn,Ti)O layer. This approach facilitates the formation of a dense ETL with precisely controllable thickness. Scanning electron microscopy (SEM) was employed to characterize the surface and cross-sectional morphology of the CZTS absorber and the complete Mo/CZTS/CdS/(Zn,Ti)O stack. As shown in Fig. 2b, the as-prepared CZTS absorber film exhibits a dense, smooth surface consisting of polycrystalline grains several hundred nanometers in lateral size. Well-defined grain boundaries are evident, with no observable pinholes, voids, or other morphological defects. This uniform microstructure results from our previously reported precursor seed layer engineering (PSLE) method for solution-processed CZTS thin film fabrication, which regulates the thermodynamic nucleation evolution of the precursor film by optimizing the hot-plate annealing duration (150 s per cycle for a total of 12 spin-coating cycles).[29] This situation is beneficial for the long-distance diffusion of carriers in the absorber and can reduce the occurrence of bulk and interfacial recombination.[30] Fig. 2c–e presents surface SEM images of the CZTS/CdS/(Zn,Ti)O stacks with varying ETL thicknesses. Samples are labeled according to the (Zn,Ti)O layer thickness, PC-1 (10 nm), PC-2 (20 nm), and PC-3 (30 nm). All stacks preserve the large-grain polycrystalline morphology of the underlying CZTS absorber, with clearly discernible grain boundaries. With increasing ETL thickness, the surface evolves from a partially covered state (PC-1) to a fully coated, continuous film (PC-3). A 10 nm (Zn,Ti)O layer (PC-1) forms a conformal coating over the CZTS/CdS heterojunction, though it only partially mitigates the substrate's inherent topological features. With increased thickness to 20 nm (PC-2), the coating densifies, exhibiting a uniform morphology characterized by refined particulate features, complete void filling, and a smoothed surface free of exposed substrate. The ultimate thickness of 30 nm (PC-3) produces a highly dense, pinhole-free (Zn,Ti)O film. This thickness, however, promotes the surface segregation of (Zn,Ti)O clusters, which induces optical opacity and severely attenuates incident light before it can reach the CZTS layer. Consequently, the morphological evolution with ETL thickness transitions sequentially from an incompletely covered state (PC-1, 10 nm) to a dense, smooth coating (PC-2, 20 nm) and finally to a slightly over-thick, agglomerated film (PC-3, 30 nm). This progression reflects a characteristic trade-off in which thicker layers improve coverage and planarization but eventually introduce excessive roughness and porosity, which may detrimentally affect interfacial recombination and carrier transport.

The cross-sectional SEM images in Fig. 2f–h corroborate these surface observations from a vertical perspective. On the surface of the precisely cleaned Mo substrate, a uniform, polycrystalline CZTS absorber layer can be observed, with grains extending throughout the full thickness of the film. This indicates that the bulk crystallization of CZTS remains consistent across the different ETL conditions. A thin ETL layer is clearly distinguishable atop the CZTS surface. All interfaces, Mo/CZTS, CZTS/CdS, and CdS/(Zn,Ti)O, are sharp and well-defined, showing no evidence of delamination or stress-induced cracking. This confirms that the deposition of CdS and (Zn,Ti)O does not induce severe interfacial degradation. As the (Zn,Ti)O thickness increases from 10 nm to 20 nm, the topmost interface becomes progressively smoother and more continuous. In the thickest sample (30 nm), localized bulges and surface accumulation are visible, consistent with the segregation of (Zn,Ti)O clusters observed in the plan-view SEM images. This vertical analysis validates the ETL evolution from incomplete coverage to a dense planar layer and finally to a slightly over-thick, agglomerated state.

To further assess the structural robustness of the optimized PC-2 photocathode under actual PEC operating conditions, post-PEC XRD characterization experiments and cross-sectional SEM were conducted on the device after the stability testing (Fig. S4). The post-PEC SEM images show that the bulk crystalline structure of the CZTS absorber and the CZTS/CdS heterojunction interface remain intact without delamination or severe damage, while only the outermost thin film layer exhibits slight degradation with a significantly rougher surface compared to the pristine state (Fig. 2d). This phenomenon is attributed to the chemical reaction of the outermost layer with the acidic electrolyte (pH = 1) during PEC operation, followed by oxidation of the damaged surface in open air during sample drying. The XRD patterns of PC-2 before and after PEC operation display consistent chalcopyrite CZTS diffraction peak positions without lattice distortion; the only changes are the reduced intensity of the main CZTS (112) peak and the emergence of a prominent SnO_2 (110) diffraction peak (its height close to the CZTS (112) peak).[31] This confirms that the tin-containing species on the degraded surface are oxidized to SnO_2 after PEC operation, and the decrease in CZTS (112) peak intensity is caused by the coverage of the SnO_2 layer rather than bulk structural damage of CZTS.

(Zn,Ti)O layers with thicknesses of 10 nm, 20 nm, and 30 nm are labeled as (Zn,Ti)O-1, (Zn,Ti)O-2, and (Zn,Ti)O-3, respectively, in the corresponding figures. The reflection spectra in Fig. 3a exhibit distinct interference oscillations, the amplitude of which increases with film thickness. The 30 nm sample shows the strongest reflection, while the 10 nm sample shows the weakest, consistent with enhanced Fabry–Pérot interference due to the greater optical path length.[32] This trend confirms the high flatness and optical uniformity of the ALD-grown (Zn,Ti)O films. However, the pronounced reflection of the 30 nm layer also introduces notable optical losses. A significant portion of incident light is reflected at the surface rather than transmitted into the CZTS absorber, thereby reducing the usable photon flux for carrier generation. The transmittance spectra (Fig. 3b) align with these observations, the 30 nm film shows substantially lower transmittance than the 10 nm and 20 nm films. The higher transmittance of the thinner layers allows more incident light to reach the CZTS absorber, enhancing light absorption and consequently increasing photogenerated charge-carrier density. Fig. 3c presents the Tauc plot from which the optical band gap (E_g) was derived using the standard Tauc relationships:[33]

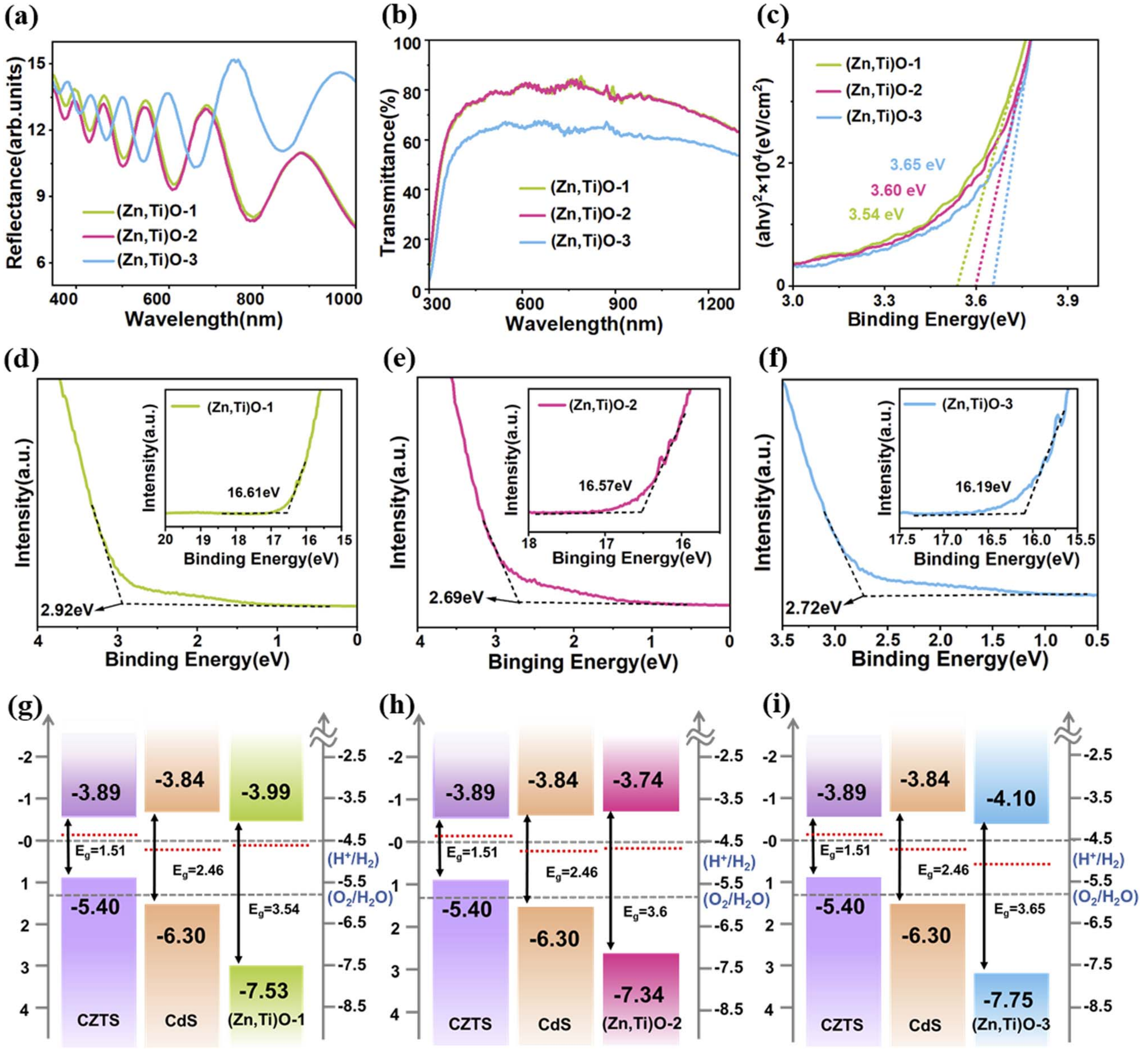

Fig. 3 (a) Reflection spectra of ETLs. (b) Transmittance spectra of the representative films. (c) Tauc plots, $(\alpha h\nu)^2$ *versus* photon energy, of the films. UPS results of (Zn,Ti)O films with thicknesses of 10 nm (d), 20 nm (e), and 30 nm (f). (g–i) Schematic representations of the conduction band minimum (E_C), valence band maximum (E_V), and bandgap (E_g) of the ETLs and CZTS absorber in devices with (Zn,Ti)O thicknesses of 10 nm (g), 20 nm (h), and 30 nm (i).

$$\alpha = d^{-1}\ln(T^{-1}) \tag{3}$$

$$\alpha h\nu = A(h\nu - E_g)^n \tag{4}$$

where d, α, T, h, ν, and n are the film thickness, absorption coefficient, transmittance, Planck's constant, photon frequency, and an exponent related to the nature of the electronic transition, respectively. The E_g value is obtained by extrapolating the linear region of the Tauc plot outward all the way to the intercept where it intersects the X-axis. The bandgap values of the extracted (Zn,Ti)O films of different thicknesses are 3.54 eV, 3.60 eV, and 3.65 eV, respectively. By increasing the thickness of (Zn,Ti)O the optical bandgap increases, a phenomenon often linked to changes in defect density and concentration of oxygen vacancies in ZTO films.[25]

To further elucidate the band alignment between CZTS/CdS and the (Zn,Ti)O ETL, Fig. 3d–i presents the UPS results of (Zn,Ti)O films with different thicknesses and the corresponding energy band diagrams. The secondary electron cutoff energy E_{cutoff} and valence-band edge E_V extracted from the UPS spectra in Fig. 3d–f were used to determine the work function and valence-band maximum of each material. Combined with the optical bandgaps E_g obtained from the Tauc plots in Fig. 3c, the conduction band minima E_C and Fermi levels E_F relative to the vacuum level were deduced.[34] On the basis of these parameters, Fig. 3g–i reconstruct the band alignment of the CZTS absorber,

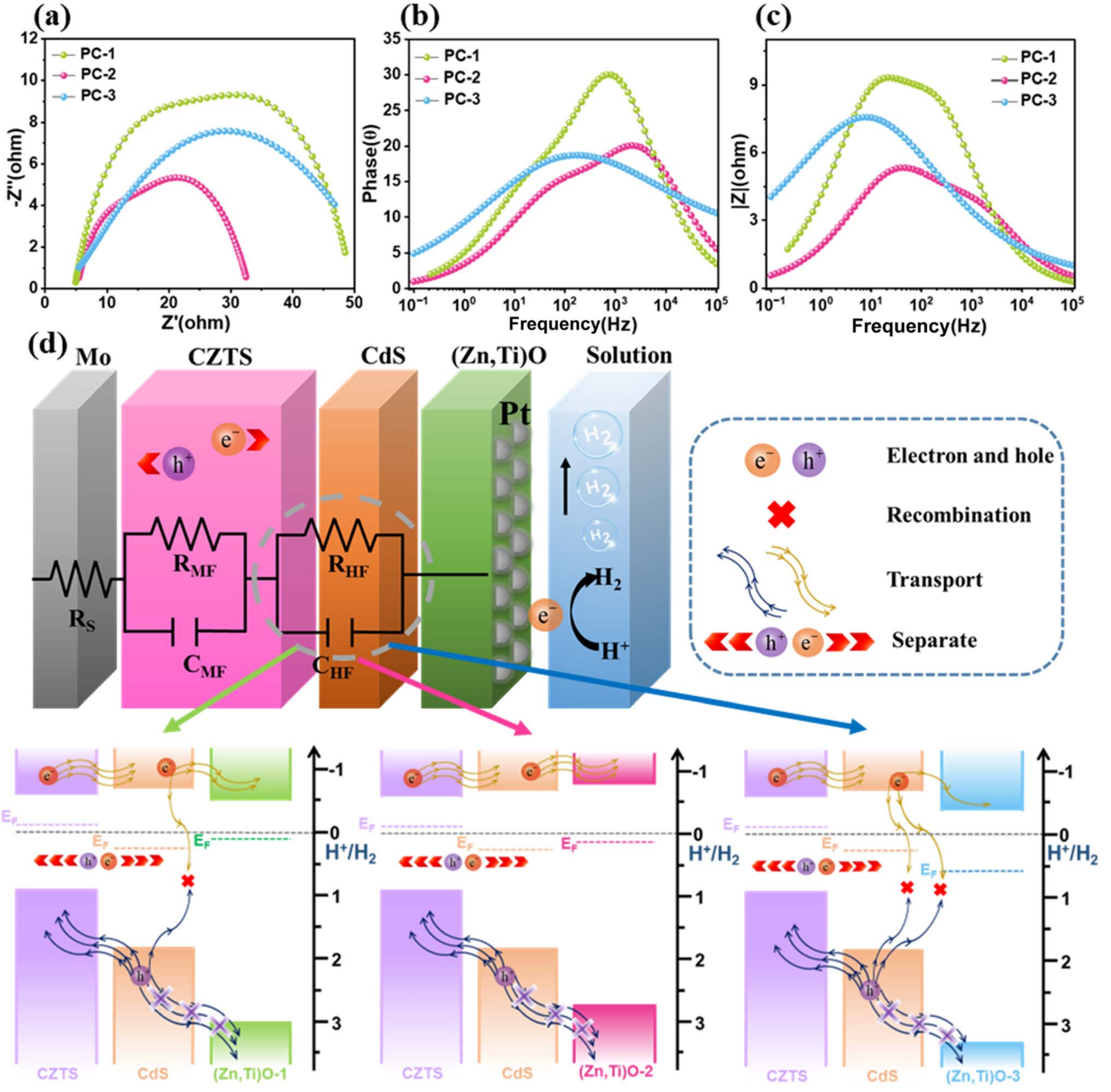

Fig. 4 PEIS analysis and equivalent circuit modeling. (a) Nyquist plots, (b) Bode phase plots, and (c) Bode magnitude plots of CZTS-based photocathodes with different (Zn,Ti)O thicknesses under illumination. (d) Schematic diagram and equivalent circuit model associated with the charge-transfer processes.

CdS buffer, and (Zn,Ti)O ETLs of different thicknesses with respect to the vacuum level, clearly illustrating the conduction-band offsets (CBOs) at various interfaces. The conduction-band positions of CZTS and CdS are approximately −3.89 eV and −3.84 eV,[29,35] respectively, yielding a small positive CBO at the CZTS/CdS interface, $\Delta E_C = E_{C,CdS} - E_{C,CZTS} \approx +0.05$ eV. This small "spike" type shift enables electrons to be effectively injected from CZTS into CdS and also provides a suitable energy barrier for holes. Unlike this situation, the CBO at the CdS/(Zn,Ti)O interface is more sensitive to the thickness of (Zn,Ti)O. The conduction-band positions of (Zn,Ti)O with thicknesses of 10, 20, and 30 nm are approximately −3.99, −3.74, and −4.10 eV, corresponding to ΔE_C (CdS/(Zn,Ti)O) values of about −0.15, +0.10, and −0.26 eV, respectively. In the cases of 10 nm and 30 nm ETLs, the negative band offset indicates the presence of a "cliff-like" band alignment phenomenon at the heterojunction interface. The cliff can act as a barrier to prevent injected electrons from passing through under forward bias conditions, which may lead to an increase in the risk of charge carrier recombination and limit the device performance.[36,37] In contrast, when the ETL is 20 nm, it presents a "spike-like" band alignment, which is conducive to promoting electron transport from the CdS buffer to (Zn,Ti)O ETLs, while minimizing charge carriers to the greatest extent.

To elucidate the influence of the (Zn,Ti)O thickness on the interfacial charge-transfer kinetics, photoelectrochemical impedance spectroscopy (PEIS) was performed on the complete Mo/CZTS/CdS/(Zn,Ti)O/Pt photocathodes (PC-1, PC-2, and PC-3) under operating conditions. The corresponding Nyquist plots (Fig. 4a) display slightly depressed semicircles within the measured potential range, which are dominated by the charge-transfer resistance at the semiconductor/electrolyte interface, with negligible contribution from the contact resistance at the absorber/ETL interface. A comparative analysis demonstrates that PC-2, modified with a 20 nm-thick (Zn,Ti)O layer, possesses the smallest semicircular arc radius. This suggests that PC-2 exhibits the lowest charge-transfer resistance among the three photocathodes, indicating the most efficient interfacial electron transfer from the PC-2 photocathode to the electrolyte. The superior kinetic performance of PC-2 reveals that the thickness of its ETL achieves an optimal balance: it provides sufficient interfacial passivation to suppress charge recombination, while minimizing resistive losses during hole blocking and electron extraction.[23] Fig. 4b shows the Bode phase plots as a function of frequency. The phase peaks of PC-1 and PC-3 are located in the range of 10^2–10^3 Hz, whereas the peak of PC-2 appears at approximately 10^4 Hz. Notably, PC-1 displays the highest and sharpest phase peak, reflecting a more uniform distribution of interfacial capacitance and a narrower distribution of time constants. PC-2 shows a similar peak height to PC-3, but its phase peak shifts distinctly toward higher frequencies, corresponding to a smaller charge-transfer time constant, which is consistent with its faster interfacial charge-transfer kinetics. The Bode magnitude spectra of the impedance modulus $|Z|$ are presented in Fig. 4c. PC-2 exhibits a markedly lower $|Z|$ than PC-1 and PC-3 across the entire measured frequency range from low to high frequencies, with the most significant difference observed in the low-frequency region (10^{-1}–10^2 Hz). These results demonstrate that the 20 nm-thick (Zn,Ti)O ETL delivers the lowest overall impedance, which stems from both the smaller charge-transfer resistance observed in the Nyquist plots and the minimal carrier transport losses. In contrast, PC-1 and PC-3 present higher impedance within the same frequency range, which is in good agreement with their larger Nyquist semicircles (increased interfacial resistance) and higher series resistance.

Based on these observed results, we used an equivalent circuit model to fit the PEIS data.[35] This equivalent circuit model is composed of a series resistor R_S and two parallel resistance-capacitor components. To be more specific, R_S is related to the resistance at the Mo/CZTS back contact interface. The high-frequency capacitance C_{HF} represents the capacitance of the space charge region. The resistance R_{HF} represents the charge transfer resistance at the CZTS/CdS/(Zn,Ti)O heterojunction. The capacitance and resistance related to defects in the intermediate frequency capacitor C_{MF} and resistance R_{MF} and CZTS absorbers are related to each other.[38] This model can effectively capture the charge transfer kinetics inside the photocathode and the behavior related to defects.

Table 1 Summary of the PEIS fitted parameters of the photocathode tested in a pH = 1 electrolyte

Device	R_S (Ω)	R_{MF} (Ω)	C_{MF} (F)	R_{HF} (Ω)	C_{HF} (F)
PC-1	7.659	42.78	0.001402	30.15	0.000346
PC-2	3.498	31.01	0.002337	22.61	0.000607
PC-3	6.913	28.27	0.00222	40.67	0.004978

The fitted parameters are shown in Table 1. The extracted equivalent-circuit parameters reveal that the series resistance (R_s) values for PC-1, PC-2, and PC-3 are 7.66 Ω, 3.50 Ω, and 6.91 Ω, respectively. These comparable values indicate consistently low ohmic losses across all devices, confirming a well-optimized and electrically benign Mo/CZTS back-contact configuration. Furthermore, PC-2 exhibits a smaller medium-frequency resistance ($R_{MF} = 31.01$ Ω), suggesting fewer bulk defects within the optimized CZTS absorber, a finding consistent with the dense, uniform morphology observed by SEM. Most notably, PC-2 demonstrates a substantially lower high-frequency resistance ($R_{HF} = 22.61$ Ω) compared to PC-1 (30.15 Ω) and PC-3 (40.67 Ω), reflecting enhanced charge-separation and transfer efficiency at the CZTS/CdS/(Zn,Ti)O heterojunction. The high-frequency capacitance (C_{HF}) increases from 3.46×10^{-4} F (PC-1) to 6.07×10^{-4} F (PC-2), then rises sharply to 4.98×10^{-3} F for PC-3. The combination of the lowest R_{HF} and a moderate C_{HF} in PC-2 indicates both low interfacial charge-transfer resistance and controlled charge accumulation. Overall, the 20 nm (Zn,Ti)O ETL achieves the optimal balance, minimizing series resistance and bulk defects while maximizing interfacial charge-separation efficiency. These favorable PEIS parameters for PC-2 directly correlate with its superior PEC performance, including higher photocurrent density and HC-STH efficiency, compared to the PC-1 and PC-3 devices.

To further investigate the correlation between the (Zn,Ti)O ETL thickness and PEC performance, Kelvin probe force microscopy (KPFM) was employed to map the surface potential distribution of the three devices. The measured contact potential difference (CPD) directly relates to the local work function and provides insights into the interfacial energy band alignment. Topography images of the three samples are shown in Fig. 5a–c. The corresponding CPD maps (Fig. 5d–f) reveal a consistent contrast between grain interiors (GIs) and grain boundaries (GBs), GIs appear brighter, indicating a higher surface potential (φ_{GI}), while GBs are darker, corresponding to a lower potential (φ_{GB}). This potential distribution can be described by the fundamental KPFM relationship.

$$\varphi_2 = \varphi_1 - eV_{CPD} \tag{5}$$

$$\varphi_2 = \varphi_1 + eV_{CPD} \tag{6}$$

$$\varphi_{GI} - \varphi_{GB} = eV_{CPD}(GB) - eV_{CPD}(GI) \tag{7}$$

where φ_1, φ_1, φ_{GI} and φ_{GB} are the potentials of the probe, sample, GIs and GBs, respectively,[39,40] e is the elementary charge, and V_{CPD} is the measured contact potential difference. The lower brightness at GBs confirms the $\varphi_{GB} < \varphi_{GI}$; this difference in work function is the driving force for downward

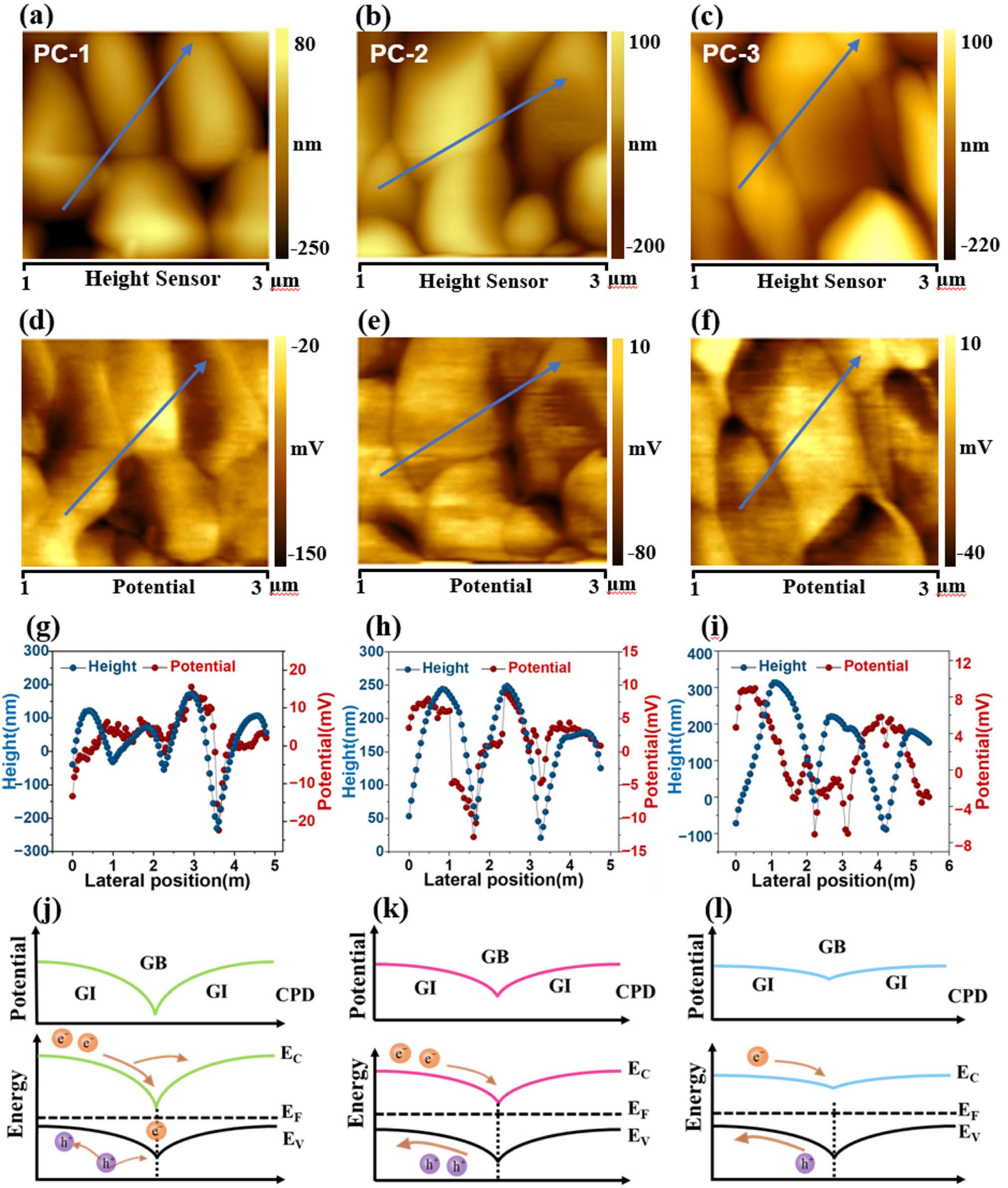

Fig. 5 KPFM characterization of Mo/CZTS/CdS/(Zn,Ti)O/Pt photocathodes. (a–c) KPFM surface morphology images, and (d–f) CPD images of Mo/CZTS/CdS/(Zn,Ti)O/Pt photocathodes with (Zn,Ti)O thicknesses of 10 nm (a and d), 20 nm (b and e), and 30 nm (c and f). (g–i) Corresponding topography and potential line-scan profiles along the white arrows in (a–c). (j–l) Schematic energy band structures and CPD distributions near grain boundaries (GBs) for the three samples.

band bending at grain boundaries. For p-type semiconductors like CZTS, this downward trend of band bending is actually a very crucial electronic feature that promotes the separation of effective carriers.[41] The line scan profiles of the AFM image and potential difference were extracted along the blue arrows in Fig. 5a–f. The results of PC-1, PC-2, and PC-3 are respectively shown in Fig. 5g–i. After observation, two repeatable trends were discovered. The first trend is that when the scanning path passes from the interior of the grain to the grain boundary, the surface height decreases, and the surface potential also drops. This confirms an intrinsic correlation between the CPD distribution and the underlying microstructure. The average potential difference between grain boundaries and interiors ($\Delta V_{\text{GB-GI}}$) was measured to be 38.57 mV for PC-1, 30.34 mV for PC-2, and 16.05 mV for PC-3. In KPFM, $\Delta V_{\text{GB-GI}}$ directly reflects the extent of downward band bending at the GBs, a larger value indicates stronger band bending, while a smaller value corresponds to weaker bending. Fig. 5j–l illustrate the corresponding band diagrams and CPD profiles near the grain boundaries for PC-1, PC-2, and PC-3, respectively. In p-type CZTS, downward band bending at GBs creates an energy barrier that confines electrons within the boundary region, restricting their random diffusion. Concurrently, holes are repelled away from the GBs, promoting electrons transport toward the electrode surface. This spatially selective band alignment effectively suppresses electron–hole recombination at the grain boundaries. However, a comparison among the three samples reveals that the magnitude of band bending must be optimized to achieve a balance between carrier separation and trap-assisted recombination. For PC-1 (Fig. 5j), the largest $\Delta V_{\text{GB-GI}}$ (38.57 mV) leads to excessive downward band bending at GBs. This relatively large degree of bending increases the local electric field. As a result, electrons are particularly prone to being captured by deep defects and recombining with holes, which significantly reduces the effective collection of charge carriers. In contrast, PC-3 (Fig. 5l), with the smallest $\Delta V_{\text{GB-GI}}$ (16.05 mV), exhibits insufficient downward band bending. The weak electric field at GBs provide insufficient driving force for effective electron–hole separation, leading to increased electron scattering and slower hole transport toward the electrode surface. This situation will increase the probability of bulk recombination of carriers before they reach the CZTS/CdS/(Zn,Ti)O interface. PC-2 (Fig. 5k) exhibits an intermediate $\Delta V_{\text{GB-GI}}$ of 30.34 mV, corresponding to moderate downward band bending that provides a sufficient electric field for efficient carrier separation while avoiding excessive electron trapping at grain-boundary defects. Overall, KPFM analysis reveals that among the three samples, the PC-2 photocathode exhibits the most favorable band bending, which simultaneously suppresses carrier recombination and promotes carrier transport. Together with its uniform ETL coverage, this optimized interfacial energetics underpins the enhanced V_{on} and HC-STH efficiency, confirming that rational band-bending engineering is a key design parameter for high-performance photocathodes.

4. Conclusion

This work establishes that precise thickness engineering of the atomic-layer-deposited (Zn,Ti)O ETL is a critical factor in unlocking the performance potential of earth-abundant CZTS photocathodes for solar water splitting. A systematic comparison of 10, 20, and 30 nm ETLs reveals that a 20 nm (Zn,Ti)O layer provides dense, uniform coverage, optimized band bending at the interface, and a favorable spike-like conduction band offset at the CdS/(Zn,Ti)O interface, enabling efficient charge separation while suppressing defect-mediated recombination. Consistently, this optimized architecture exhibits the lowest charge-transfer resistance and delivers a high photocurrent density of 29.2 mA cm^{-2} at 0 V$_{\text{RHE}}$ with a half-cell solar-to-hydrogen efficiency of 7.02%. KPFM analysis further reveals that this performance enhancement originates from optimized interfacial band bending and a uniform surface potential distribution, which together facilitate efficient charge separation and transport. These findings underscore that meticulous ETL thickness control is essential for optimizing band alignment and charge management in chalcogenide-based thin film photoelectrodes, providing a general strategy for efficient solar fuel systems based on earth-abundant materials.

Author contributions

G. L., S. C., and M. A. conceived the original concept and designed the experiments. G. L., and S. C. supervised and guided the entire project. S. R. conducted the experiments. M. A., and S. R. analysed the data and wrote this manuscript. Z. X., Z. L., and J. Y. helped in device performance characterizations.M. I., Z. Z., and J. Z. aided in device structural characterization. G. L., and S. C. co-revised the manuscript. All authors commented on the manuscript.

Conflicts of interest

The authors declare no conflict of interest.

Data availability

The data supporting this article are available from the corresponding authors upon request.

Supplementary information (SI): faradaic efficiency graph, XRD patterns of the photocathodes before and after PEC operation, EDS analysis, and post-PEC SEM images. See DOI: https://doi.org/10.1039/d6sc00648e.

Acknowledgements

This work was supported by the National Natural Science Foundation of China (no. 62474114), Guangdong Basic and Applied Basic Research Foundation (2025A1515011515) China, Science and Technology plan project of Shenzhen (JCYJ20240813141620027) China, and Shenzhen University 2035 Program for Excellent Research (grants 2024B003).

References

1 F. N. I. Sari, P.-C. Chuang, S.-C. Huang, C.-Y. Lin and Y.-H. Lai, *Chem. Sci.*, 2025, **16**, 13966–13996.
2 H. Wu, P. Guo, Y. Tang, H. Li and R. Mo, *Appl. Phys. Lett.*, 2025, **127**, 163902.
3 F. Amano and K. Tsushiro, *Energy Mater.*, 2024, **4**, 400006.

4 T. Hisatomi, T. Yamada, H. Nishiyama, T. Takata and K. Domen, *Nat. Rev. Mater.*, 2025, **10**, 769–782.

5 B. Chandran, J.-K. Oh, S.-W. Lee, D.-Y. Um, S.-U. Kim, V. Veeramuthu, J.-S. Park, S. Han, C.-R. Lee and Y.-H. Ra, *Nano-Micro Lett.*, 2024, **16**, 244.

6 A. Fujishima and K. Honda, *Nature*, 1972, **238**, 37–38.

7 B. Zhang, Z. Fan and Y. Li, *Sci. China Chem.*, 2024, **67**, 2171–2180.

8 T. Hisatomi and K. Domen, *Nat. Catal.*, 2019, **2**, 387–399.

9 J. Ke, F. He, H. Wu, S. Lyu, J. Liu, B. Yang, Z. Li, Q. Zhang, J. Chen, L. Lei, Y. Hou and K. Ostrikov, *Nano-Micro Lett.*, 2020, **13**, 24.

10 K. J. Jenewein, J. Knöppel, A. Hofer, A. Kormányos, B. Mayerhöfer, F. D. Speck, M. Bierling, S. Thiele, J. Bachmann and S. Cherevko, *SusMat*, 2023, **3**, 128–136.

11 M. Chen, Y. Liu, C. Li, A. Li, X. Chang, W. Liu, Y. Sun, T. Wang and J. Gong, *Energy Environ. Sci.*, 2018, **11**, 2025–2034.

12 J. Tan, B. Kang, K. Kim, D. Kang, H. Lee, S. Ma, G. Jang, H. Lee and J. Moon, *Nat. Energy*, 2022, **7**, 537–547.

13 J. Tan, W. Yang, H. Lee, J. Park, K. Kim, O. S. Hutter, L. J. Phillips, S. Shim, J. Yun, Y. Park, J. Lee, J. D. Major and J. Moon, *Appl. Catal., B*, 2021, **286**, 119890.

14 J. Li, J. Huang, F. Ma, H. Sun, J. Cong, K. Privat, R. F. Webster, S. Cheong, Y. Yao, R. L. Chin, X. Yuan, M. He, K. Sun, H. Li, Y. Mai, Z. Hameiri, N. J. Ekins-Daukes, R. D. Tilley, T. Unold, M. A. Green and X. Hao, *Nat. Energy*, 2022, **7**, 754–764.

15 X. Zhao, J. Li, C. Hu, Y. Qi, Z. Zhou, D. Kou, W. Zhou, S. Yuan and S. Wu, *Nano-Micro Lett.*, 2024, **17**, 84.

16 J. Shi, J. Wang, F. Meng, J. Zhou, X. Xu, K. Yin, L. Lou, M. Jiao, B. Zhang, H. Wu, Y. Luo, D. Li and Q. Meng, *Nat. Energy*, 2024, **9**, 1095–1104.

17 M. Zhang, P. Yang, W. Tao, X. Pang, Y. Su, P. Peng, L. Zheng, R. Li, S. Wang, J. Huang, L. Zou and J. Xie, *Energy Mater.*, 2024, **4**, 400028.

18 Y. Yang, Y.-X. Chen, A.-S. She, H.-Y. Shi, W. Chen, W. Wang, H.-L. Wang, K.-X. Li, Y.-H. Pu, W.-H. Yang, X.-M. Lin and C.-Z. Lu, *Chin. J. Struct. Chem.*, 2025, **44**, 100623.

19 G. T. Chavan, Y. Kim, M. Q. Khokhar, S. Q. Hussain, E.-C. Cho, J. Yi, Z. Ahmad, P. Rosaiah and C.-W. Jeon, *Nanomaterials*, 2023, **13**, 1226.

20 Y.-H. Liao, Y.-H. Chang, T.-H. Lin, K.-M. Lee and M.-C. Wu, *Materials*, 2024, **17**, 2722.

21 I. Adinata, A. A. Pringgodani, M. P. Nobel, G. E. Timuda and T. Tulus, *Nanoscale*, 2026, **18**, 2798–2810.

22 P. Shinde, Y. Hase, V. Doiphode, B. R. Bade, D. Kale, S. Rahane, J. Thombare, D. Borkar, S. R. Rondiya, M. Prasad, S. P. Patole and S. R. Jadkar, *ACS Appl. Energy Mater.*, 2025, **8**, 935–948.

23 M. Ma, Y. Huang, J. Liu, K. Liu, Z. Wang, C. Zhao, S. Qu and Z. Wang, *J. Semicond.*, 2020, **41**, 091702–091713.

24 J.-S. Kim, J.-K. Kang and D.-K. Hwang, *APL Mater.*, 2016, **4**, 096101.

25 S. Chen, Y. Chen, H. Zhang, M. Abbas, D. Ren, Y. Chen, J. Luo, Z. Zheng, Z. Su and G. Liang, *Adv. Mater.*, 2026, e18202.

26 A. Usman and T. Bovornratanaraks, *ACS Omega*, 2024, **9**, 39663–39672.

27 Q. Fatima, A. A. Haidry, H. Zhang, A. El Jery and M. Aldrdery, *Mater. Today Sustain.*, 2024, **27**, 100857.

28 W. Yang, J. H. Kim, O. S. Hutter, L. J. Phillips, J. Tan, J. Park, H. Lee, J. D. Major, J. S. Lee and J. Moon, *Nat. Commun.*, 2020, **11**, 861.

29 M. Abbas, S. Chen, Z. Li, M. Ishaq, Z. Zheng, J. Hu, Z. Su, Y. Li, L. Ding and G. Liang, *Nano-Micro Lett.*, 2025, **17**, 257.

30 S. D. Stranks, G. E. Eperon, G. Grancini, C. Menelaou, M. J. P. Alcocer, T. Leijtens, L. M. Herz, A. Petrozza and H. J. Snaith, *Science*, 2013, **342**, 341–344.

31 H. Du, H. Yu, D. K. Macharia, H. Zeng, H. Wang, R. Cao, N. Yu, M. Zhu and Z. Chen, *J. Colloid Interface Sci.*, 2025, **689**, 137195.

32 L. Chen and Q. Wu, *Sci. Rep.*, 2025, **15**, 6419.

33 G. P. Joshi, N. S. Saxena, R. Mangal, A. Mishra and T. P. Sharma, *Bull. Mater. Sci.*, 2003, **26**, 387–389.

34 X. Zhang, C. Blackman, R. G. Palgrave, S. Ashraf, A. Dey, M. O. Blunt, X. Zhang, T. Liu, S. Sun, L. Zhu, J. Guan, Y. Lu, T. W. Keal, J. Buckeridge, C. R. A. Catlow and A. A. Sokol, *J. Am. Chem. Soc.*, 2024, **146**, 16814–16829.

35 G. Liang, Z. Li, M. Ishaq, Z. Zheng, Z. Su, H. Ma, X. Zhang, P. Fan and S. Chen, *Adv. Energy Mater.*, 2023, **13**, 2300215.

36 S. Chen, Y. Chen, H. S. Aziz, H.-H. Zhang, Z.-L. Li, Y.-X. Chen, Y.-J. Zeng, Z.-H. Zheng, J.-G. Hu, Z.-H. Su and G.-X. Liang, *Adv. Funct. Mater.*, 2025, **35**, 2420912.

37 Y. Gong, Q. Zhu, B. Li, S. Wang, B. Duan, L. Lou, C. Xiang, E. Jedlicka, R. Giridharagopal, Y. Zhou, Q. Dai, W. Yan, S. Chen, Q. Meng and H. Xin, *Nat. Energy*, 2022, **7**, 966–977.

38 F. Zhao, X. Ning, L. Xu, P. Chen, Z. An and X. Chen, *Chin. Chem. Lett.*, 2025, 112026.

39 W. Zhao, T. Wu, I. P. Perera, Y. Dang, I. T. Olowookere, Q. Luo, H. Tan, D. Silva and S. L. Suib, *J. Mater. Chem. A*, 2025, **13**, 14216–14228.

40 Y. Zhang, Z. Zou, Q. Liu, Y. Qiao and C. Jiang, *J. Mater. Sci. Technol.*, 2025, **221**, 278–288.

41 W. Li, W. Li, G. Chen, L. Wu, J. Zhang, M. Chen, G. Zhong, J. Zhu, Y. Feng, H. Zeng and C. Yang, *ACS Nano*, 2023, **17**, 15742–15750.